Mapping Fractures using MicroCT Images

Omar Alamoudi

May 14, 2019

A comment Nicola made during our meeting

We should measure the point spread function, or edge spread function of our machine using properly calibrated materials (standard point, or cube, or bar) and use the resultant estimate of the point spread function in the image analysis.

1 Introduction

In applications that are relevant to the utilization and understanding composite materials, particularly multi-phase materials, understanding the effective or apparent properties of such composites is essential for understanding how they behave under the influence of different physical and chemical processes. It is also very important to understand how constituents of such composites affect one another along the surfaces of contact. Rocks, soils, and rock melts are three complex composite material examples that geologist, geophysicists, and engineers encounter. Rocks are very rarely composed of a single physical material phase, in most likelihood, a rock sample is composed of at least two phases: a solid, and a fluid phase. The interaction between these phases is governed by the physical properties of each phase, and the law of conservation of mass, momentum, and energy of their system. With this broad view points in mind, a particular physical process that I am interested in is the processes governing fluid flow within fractured rocks, how the flow is affected by the introduction of fractures in such rocks, and the influence of varying the fluid pressure on these fractures, their capacity of storage and the flow of the fluids through them.

Darcy's law shown in Eq. (1) (Darcy 1856; Mavko et al. 2009) governs the conductivity of fluid within a cylindrical porous material sample with known geometry. The driving force of the fluid motion is the pressure gradient. Darcy's law does not make any explicit declarations about the spatial distribution, or shape of the pores within a rock specimen. On the other hand, the Kozeny–Carman (Carman 1961; Mavko et al. 2009) describes the fluid flow through a cylindrical cavity in solid block see Eq. (2). Imagine drilling a cylindrical cavity in the cylindrical sample with the known geometry with Radius R. Equation (2) describes the flow through that cavity.

$$Q = -\frac{A}{L}\frac{\kappa}{\mu}\Delta p \tag{1}$$

$$Q = -\frac{1}{L}\frac{\pi R^4}{8\mu}\Delta p \tag{2}$$

$$\kappa = \frac{\pi R^4}{8A} \tag{3}$$

Comparing Eq. (1) and Eq. (2), Eq. (3) shows that there a dependence of permeability on the cross sectional area of the sample, and the radius of the cavity. Considering an alternative case where we have fractures, one can deduce that we can estimate or predict the relationship between a rock sample geometry and fractures within the sample that would be the primary conduit of fluid flow. Therefore, the use of microCT images to map fractures is an important first step to understanding such relationship.

Considering a single two-dimensional slice from a three-dimensional microCT volume data of two half-cylinder of a rock sample, Ketcham et al. 2010 have demonstrated the applicability of what the authors call the Inverse Point Spread Function method (IPSF) in measuring the apparent and true aperture of fractures from microCT volumes. Using this method requires visually inspecting and detecting the fractures in the image, then measuring them. An alternative approach proposed by Voorn et al. 2013 employs computing the Hessian to detect multi-scale fractures within a sample. In the paper, we discuss the application of Voorn et al. 2013 approach on synthetic images as a first step in attempting to detect fractures with the aim to eventually measure them.

2 Methods

Our main objective is to improve the ability to detect, and henceforth measure fractures in microCT images acquired of rock samples. The approach followed is a similar to, if not the same as, the one described in Voorn et al. 2013. To demonstrate this approach in detecting fractures, computed the Hessian of the synthetic images, and finally conducted analysis to map the fracture features from the images. The description of these steps follows in the same order stated above.

2.1 Synthetic Image Generation

The workflow used in generating the synthetic fracture images was done using MATLAB. A user specified array of fracture apertures specified as an integer of pixels/voxels, i.e. [1,2,3,4,6] as shown in Fig. (1), an integer number of pixels/voxels representing the length and width of the desired image, and an estimate of the signal to noise ratio (SNR) are used as input arguments. An equally spaced fractures are drawn in an image as pixels with the gray value zero in a background with gray value one. Four different images are generated in two sets. The first set is of two "sharp" images, and the other two are blurred by convolving the sharp image with a 3-by-3 (-by-3 in 3D) box filter. The blurred images are an attempt to represent the effect of the Point Spread Function (PSF) of a microCT machine (Ketcham et al. 2010). Random noise was added to one of each set to observe and quantify the effect of random noise. The result of this workflow is a two-dimensional image with the specified fractures apertures as the apparent fractures, but since our objective is to map fractures, a plate like geometrical features, Voorn et al. 2013 have stated that two-dimensional images are insufficient in mapping fractures. To generate a three-dimensional image with fractures that are vertically oriented, a stack of three of same image are superimposed on one another. For the images that contain noise, three different realizations of noise are stacked to preserve the randomness of noise. Figure (1) shows the middle slice of a three-dimensional image with input parameters [1,2,3,4,6] for fracture apertures, 100 voxels for the length of the image, and 10 for the SNR.

2.2 Computing the Hessian

To compute the Hessian of a microCT image, consider a three dimensional Euclidean domain E^3 representing the domain of a microCT image, and given a scalar valued field $\phi : E^3 \to \mathbb{R}$ representing the gray value of every voxel. The Hessian of the scalar field ϕ is $\mathbf{H}(\phi)$ as shown in Equation (4).

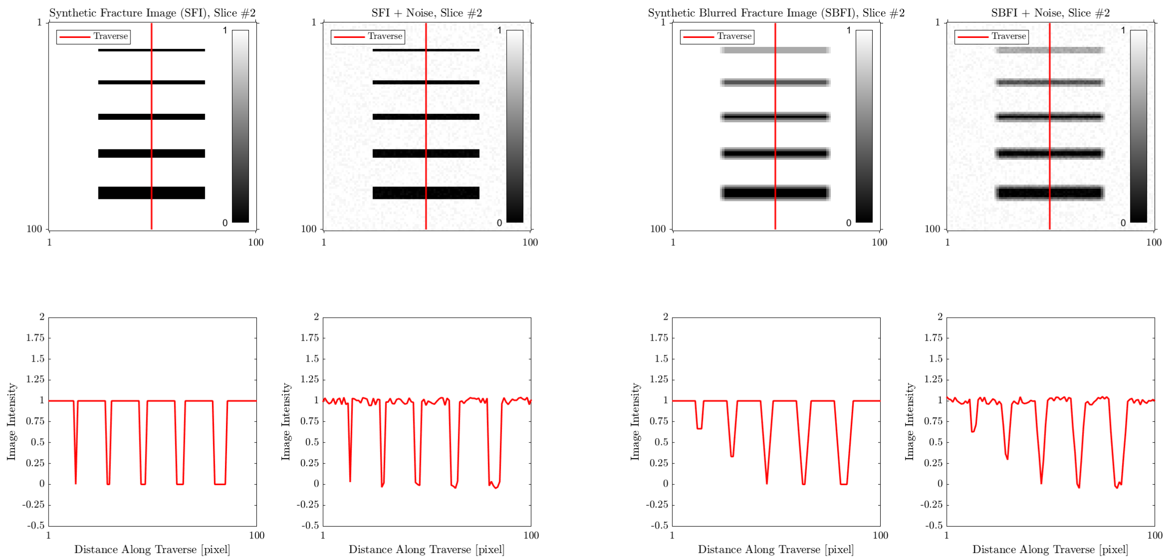

(a) Set of "sharp" images

(b) Set of blurry images

Figure 1: The middle slice of a three-dimensional synthetic images. Top row shows the images, and the bottom row shows a traverse along the vertical red line.

$$\mathbf{H} = \begin{bmatrix} I_{xx} & I_{xy} & I_{xz} \\ I_{yx} & I_{yy} & I_{yz} \\ I_{zx} & I_{zy} & I_{zz} \end{bmatrix} \tag{4}$$

Where

$$I = \text{microCT image gray value field or image intensity}$$
$$I_{ij} = \frac{\partial}{\partial i}\frac{\partial}{\partial j} I. \qquad i, j = [x, y, z] \tag{5}$$

The Hessian is a tensor value function $\mathbf{H} : E^3 \to \mathbb{R}^3 \times \mathbb{R}^3$. It has nine components six of which are unique, as the Hessian is symmetric. Organizing the Hessian componenets in a 3-by-3 matrix, H_{ij} denotes the component of the ith row and jth column where $i, j = [x, y, z]$. Here x, y, and z are orthogonal coordinates of our Euclidean space E^3. Since microCT images, or digital images in general, are discrete in nature, the computation of the derivatives can be done by finite differences. But that is not adequate. A *multi-scale* technique is rather used. An over view of such technique is provided by Lindeberg 1998. This technique considers different scales of particularly edge features, in our case represented by fractures. For example, the second derivative $I_{xy} = \frac{\partial}{\partial x}(\frac{\partial I}{\partial y})$ of a three-dimensional image represented by $I = I(x, y, z)$ is computed as following:

$$I_{xy} = \alpha \left[I * G_{xy}(x, y, z, s) \right] \tag{6}$$

Where

$$\alpha = \text{Normalization factor}$$

$$G(x, y, z, s) = \beta \exp\left\{ -\frac{1}{2s^2} \left[(x - x_0)^2 + (y - y_0)^2 + (z - z_0)^2 \right] \right\} \quad \text{(Gaussian)}$$

$$\beta = \text{Amplitude of the Gaussian, normalization factor}$$

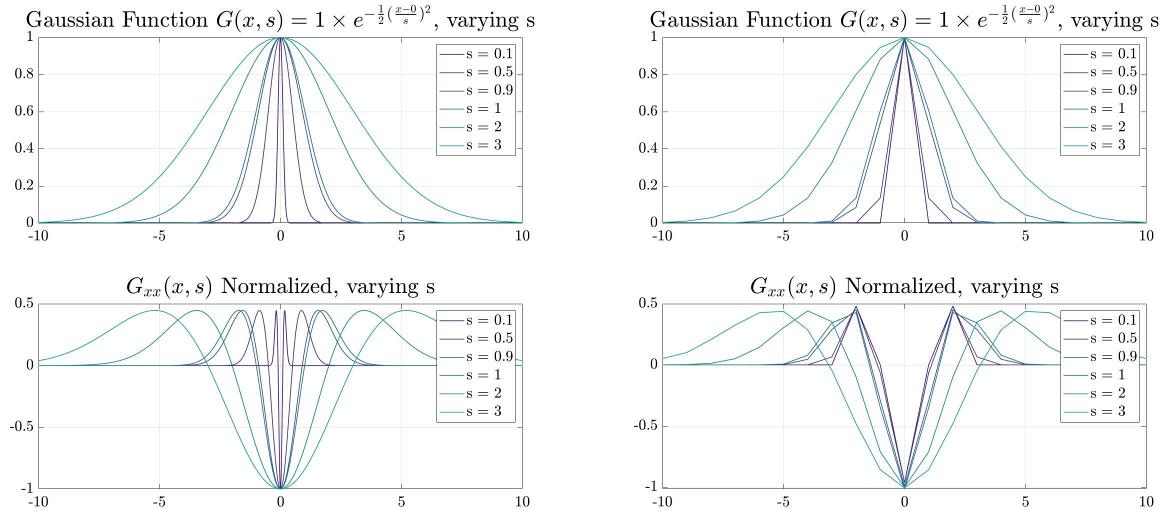

(a) Continuous

(b) Discrete

Figure 2: One-dimensional Gaussian function and $G_x x(x, s)$ with varying s in continuous and discrete forms.

Figure (2) shows a one-dimensional Gaussian function and the second derivative with respect to x in a continuous and a discrete form. The second derivative is equivalent to the G_{xx} component that is convolved with the intensity of the image as shown in Eq. (6). It is important to note that all of the operations carried out here is done using the discrete form. Different curves in Fig. (2) correspond to a different scaling parameter s. Darker colors correspond to small s, while brighter colors correspond to a larger s.

For every single synthetic image of the set generated, we computed the all nine components of the Hessian for each voxel for different values of the scaling parameter s. This was done by first choosing a value of s, then generating a three-dimensional Gaussian filter, $G(x, y,)$, using the MATLAB function `fspecial3` with a *filter size of 19*, computing the nine derivatives, $G_{ji}(x, y, x)$ for $i, j = [x, y, z]$, that are used in Eq. (6), then convolving the result with the images while choosing α such that Looking at the bottom plot of Fig. (2a), each curve can be defined by it largest trough bounded by two smaller peaks. The distance that defines the largest trough for every curve between the two points (closest to zero) intersection the horizontal axis is $2s$.

2.3 Fracture Mapping Analysis

After computing the all nine components of the Hessian for every voxel of the synthetic images for every value of s, we compute the eigenvalues $\lambda_1,\ \lambda_2,\ \lambda_3$, where $\lambda_1 < \lambda_2 < \lambda_3$. For every value of s, for plate like features, we expect one of the eigenvalues to have a large magnitude while the other two to have small magnitudes. Using the same criteria proposed by Voorn et al. 2013, we can then define a new value A_s for every voxel such that

$$A_s = \begin{cases} \lambda_3 - |\lambda_2| - |\lambda_1| & \text{if } (\lambda_3 - |\lambda_2| - |\lambda_1|) > 0 \\ 0 & \text{otherwise} \end{cases}$$

where s here stands for the scaling parameter. We then normalize A_s such that $B_s = \frac{A_s}{\max(A_s)}$, and finally define another quantity C_s such that

$$C_s = \begin{cases} 1 & \text{if } B_s > 1 - \gamma \\ 0 & \text{otherwise} \end{cases}$$

γ is an arbitrary tolerance that I chose to be 0.40 in my application. I then summed up all of C_s for all scaling parameters used. In my case, since this analysis was applied to a synthetic image set, the scaling parameter was set to be $s = \frac{1}{2}[1, 2, 3, 4, 6]$. Figure (3) shows the results of conducting the above steps for every value s.

The final step is normalizing the final cumulative result shown in Fig. (3), and inverting the image to match the original synthetic image as shown in Fig. (4).

3 Results and Discussion

Figure (4) shows the result of my analysis on all four synthetic images. We can see from the traverse profiles that we are able to detect the fractures of different scales in the sharp images, but we are unable to detect the smallest fracture in the blurred images. We can also see that the effect of random noise with SNR = 10 on the final result is minimal. Although we are able to detect the fractures, the fracture apertures do not visually match the corresponding fractures in the original synthetic image.

Since our data set and kernels used in the convolution operation are made out of discrete values, the shape of our filters used in the convolution operation shown in Fig. (2b) must be preserved. This means that when using the MATLAB function `fspecial3` to generate the 3D filter, one needs to plot it and insure that the size of the filter results in filter shape that preserves the two-peak-one-trough shape for a specific scaling parameter s. To show this better, considering a 2D filter that is easier to visualize. Figure (5) shows the kernel generated using the *gaussian* option of the MATLAB function `fspecial2` (2D equivalent of `fspecial3`). Shown in this figure are four different filters for one scaling parameter $s = 1$. The sizes shown are 5, 9, 11, and 19. Figure (5a) shows that the second derivative G_{xx} shown in the right column does not preserver the trough-peak-trough shape required to produce the appropriate results. But a filter size of 9 or greater seem to preserve that shape, making such sizes adequate to produce the correct results. The main advantage of keeping the filter size small however, is reducing the computing expense. For my synthetic images, which are 100 x 100 x 3 voxels in size, the computational time was minimal, but considering an actual image of a rock, the computations could become very expensive. An attempt that is not shown here on an image of size 1000 x 350 x 3 was made, and the computational time was about 15 minutes. This shows that there should be an optimal filter size for every scaling parameter s to optimize the computational expense.

4 Conclusions

The approach proposed by Voorn et al. 2013 seems to be successful at detecting fractures of multiple scales. There are a few parameters in the algorithm, such as the tolerance parameter γ used in computing C_s that require some trial and error to optimize the results. In my analysis, it was not possible to recover the fracture apertures from the results, that can be due to the small size of the images used. Further analysis on larger synthetic images and microCT rock images can be used to optimized the approach further. The size of the filters used in the computation of the Hessian are critical to produce correct results. Finally, further investigations into optimizing this approach to recover the fracture apertures is of value and will be considered in future work.

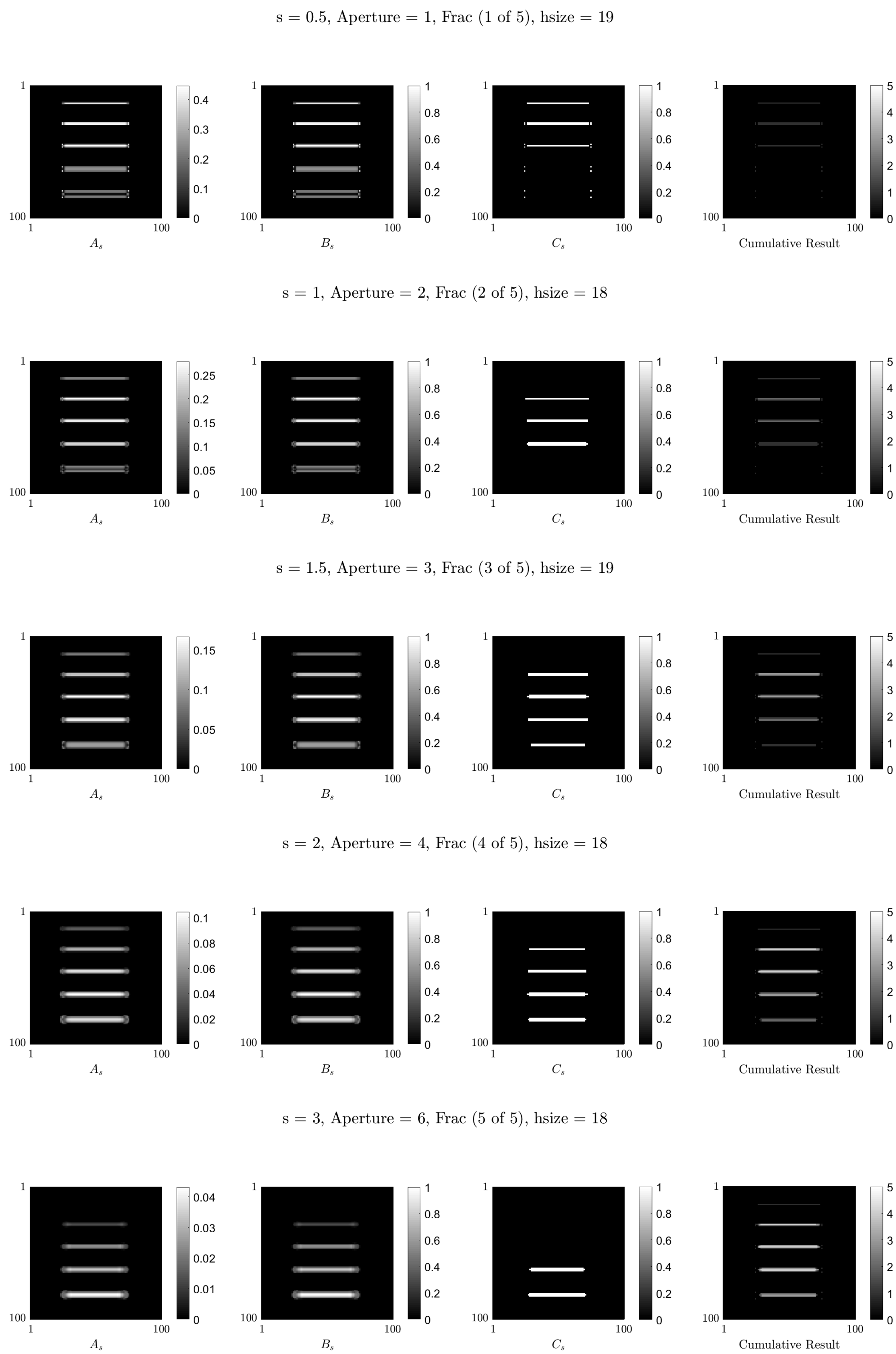

Figure 3: From top to bottom, incremental results for every scaling value s. Left to right of each row A_s, B_s, C_s, and the cumulative addition of the current step and all of the previous ones of C_s. Note here that the bottom row shows the final result of the analysis before normalizing and inverting the image.

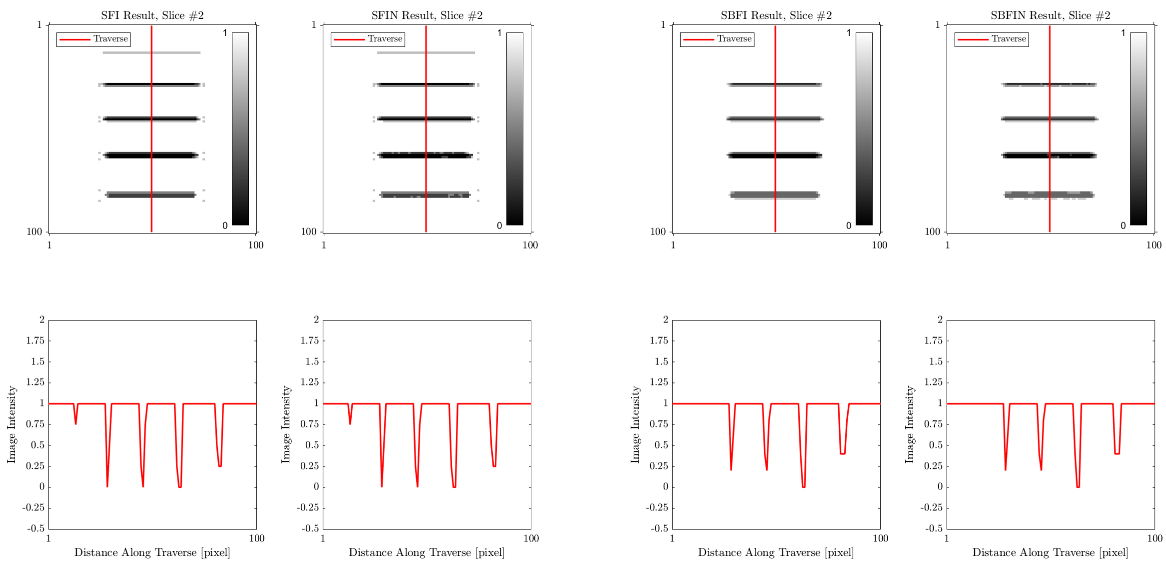

(a) Result set of ”sharp” images

(b) Result set of blurry images

Figure 4: The middle slice of a three-dimensional resultant images. Top row shows the images, and the bottom row shows a traverse along the vertical red line.

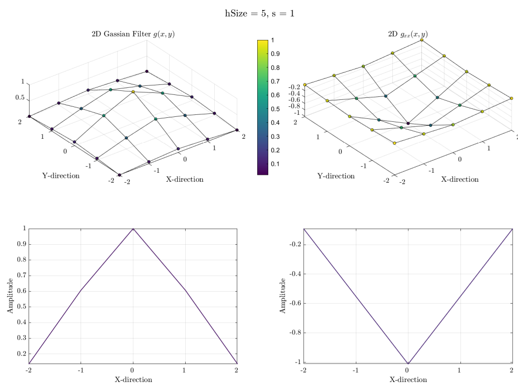

(a) Filter size = 5

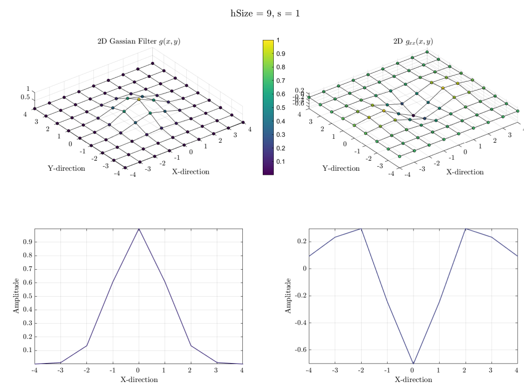

(b) Filter size = 9

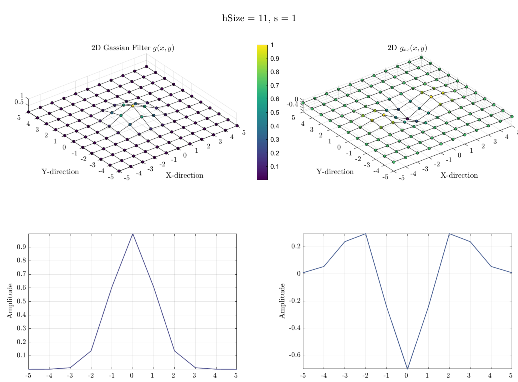

(c) Filter size = 11

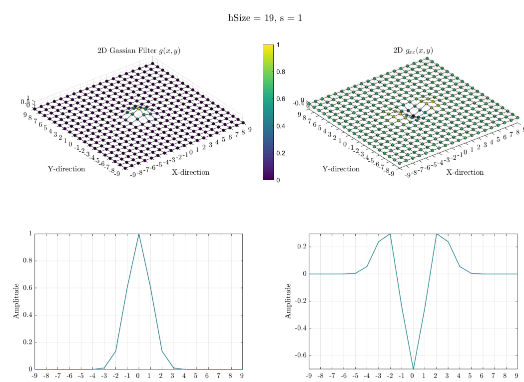

(d) Filter size = 19

Figure 5: Two-dimensional Gaussian filter $G(x, y)$ (top left of each set), and $G_{xx}(x, y)$ (top right of each set) for $s = 1$ and different filter sizes used in generating the kernels by the MATLAB function `fspecial3`. The bottom row of each set is a traverse line along a line with y-axis value = 0.

References

Carman, PC (1961). "L'ecoulement des gaz a travers les milieux poreux: Presses Universitaires de France". In:

Darcy, Henry Philibert Gaspard (1856). *Les Fontaines publiques de la ville de Dijon. Exposition et application des principes à suivre et des formules à employer dans les questions de distribution d'eau, etc.* V. Dalamont.

Ketcham, Richard A. et al. (2010). "Three-dimensional measurement of fractures in heterogeneous materials using high-resolution X-ray computed tomography". In: *Geosphere* 6.5, pp. 499–514. DOI: `10.1130/ges00552.1`.

Lindeberg, T. (1998). "Edge detection and ridge detection with automatic scale selection". In: 30.2, pp. 117–154. DOI: `10.1023/A:1008097225773`. URL: `https://doi.org/10.1023/A:1008097225773`.

Mavko, Gary et al. (2009). *The Rock Physics Handbook.* Cambridge: Cambridge University Press, p. 511. ISBN: 9780511626753. DOI: `10.1017/CBO9780511626753`. URL: `http://ebooks.cambridge.org/ref/id/CBO9780511626753`.

Voorn, Maarten et al. (2013). "Multiscale Hessian fracture filtering for the enhancement and segmentation of narrow fractures in 3D image data". In: *Computers and Geosciences* 57, pp. 44–53. ISSN: 00983004. DOI: `10.1016/j.cageo.2013.03.006`. URL: `http://dx.doi.org/10.1016/j.cageo.2013.03.006`.